Title

Real time imaging of two-dimensional iron oxide spherulite nanostructure formation

Journal

Nano Research, 12(11)

ISSN

1998-0124

Authors

Zheng, Wenjing
Hauwiller, Matthew R
Liang, Wen-I
et al.

Publication Date

2019-11-01

DOI

10.1007/s12274-019-2531-4

Peer reviewed

Real Time Imaging of Two-Dimensional Iron Oxide Spherulite Nanostructure Formation

Wenjing Zheng[1,2], Matthew R. Hauwiller[2,3], Wen-I Liang[2,4], Colin Ophus[5], Peter Ercius[5], Emory M. Chan[5], Ying-Hao Chu[4], Mark Asta[2,6], Xiwen Du[1](✉), A. Paul Alivisatos[2,3,7], Haimei Zheng[2,6](✉)

[1] *Institute of New-Energy Materials, School of Materials Science and Engineering, Tianjin University, Tianjin 300350, China.*

[2] *Materials Sciences Division, Lawrence Berkeley National Laboratory, Berkeley, CA, 94720, USA.*

[3] *Department of Chemistry, University of California, Berkeley, California, 94720, USA*

[4] *Department of Materials Science and Engineering, National Chiao Tung University, Hsinchu, 30010, Taiwan*

[5] *The Molecular Foundry, Lawrence Berkeley National Laboratory, Berkeley, CA, 94720, USA*

[6] *Department of Materials Science and Engineering, University of California, Berkeley, CA, 94720, USA*

[7] *Kavli Energy NanoScience Institute, University of California-Berkeley and Lawrence Berkeley National Laboratory, Berkeley, CA, 94720, USA*

Address correspondence to XiWen Du. xwdu@tju.edu.cn; Haimei Zheng, hmzheng@lbl.gov

ABSTRACT

The formation of complex hierarchical nanostructures has attracted a lot of attention from both the fundamental science and potential applications point of view. Spherulite structures with radial fibrillar branches have been found in various solids; however, their growth mechanisms remain poorly understood. Here, we report real time imaging of the formation of two-dimensional (2D) iron oxide spherulite nanostructures in a liquid cell using transmission electron microscopy (TEM). By tracking the growth trajectories, we show the characteristics of the reaction front and growth kinetics. Our observations reveal that the tip of a growing branch splits as the width exceeds certain sizes (5.5-8.5 nm). The radius of a spherulite nanostructure increases linearly with time at the early stage, transitioning to nonlinear growth at the later stage. Furthermore, a thin layer of solid is accumulated at the tip and nanoparticles from secondary nucleation also appear at the growing front which later develop into fibrillar branches. The spherulite nanostructure is polycrystalline with the co-existence of ferrihydrite and Fe_3O_4 through-out the growth. A growth model is further established, which provides rational explanations on the linear growth at the early stage and the nonlinearity at the later stage of growth.

KEYWORDS

liquid cell TEM, in situ TEM, iron oxide, spherulite nanostructures

1 Introduction

Solid precipitation from a liquid precursor solution can produce nanostructures with various morphologies, such as nanocrystals with well-defined shapes, as well as dendrites and spherulites of complex hierarchical nanostructures. Spherulites are two- or three-dimensional (2D or 3D) branched solids with nearly spherical external shape but notable internal surfaces. In contrast to dendritic structures with fractal branches, spherulites have more densely packed fibrillar branches. During the formation of spherulites, the fibrillar branches grow predominantly in radial directions from a common center point. Spherulites have been found in a wide range of solids from metals and alloys [1] to polymers [2], oxides [3, 4], minerals [5, 6], liquid crystals [7-9] and various biological molecules [10]. Quenching of a liquid may also lead to spherulite formation [11-13]. The prevalence of spherulites has attracted significant interest in the study of their formation mechanisms.

Previous studies have compared the growth of dendrites and spherulites, since a system may develop into either dendrite or spherulite morphology by varying the growth parameters only slightly [14, 15]. However, the growth mechanisms of spherulites are less explored than the dendrite growth with well-developed theories [16-28]. A number of phenomenological models and simulation [8, 9, 14, 29-31] have elucidated the physical requirements associated with spherulite formation. A set of factors have been identified to be critical to spherulite growth, for example, a high supercooling or oversaturation [14, 32], the occurrence of secondary nucleation at the growth front [33-37], and so on. To date, previous studies of spherulite growth have focused primarily on microscale phenomena, and a deeper understanding of spherulite formation is needed, particularly on the nanoscale.

Here, we directly visualize the spherulite nanostructure formation with in situ liquid cell transmission electron microscopy (TEM). The development of advanced liquid cell TEM has opened opportunities to address many scientific problems in broad areas of research ranging from materials science to chemistry and biology [38-41]. Liquid cell TEM offers unique advantages in allowing the direct observation of dynamic phenomena in liquids with atomic resolution and millisecond temporal resolution. With self-contained liquid cells, we previously directly studied one-dimensional nanocrystal growth by nanoparticle attachment [42, 43], the role of coalescence in nanocrystal growth [42], the dominant effects of ligand mobility on nanocrystal shape evolution [44], and the reversible giant deformation of semiconductor nanocrystals during superlattice transformations [45] and so on. With iron oxide as a model system, we have also studied the formation of nanodendrites [46]. We found that the growth of nanodendrites is consistent with the theoretical predictions of dendrite morphology evolution, demonstrating that liquid cell TEM studies allow direct assessing classical dendrite theories at the nanoscale.

In this work, liquid cell TEM is used to study the growth of spherulite nanostructures and the growth dynamics with an unprecedented level of detail. By imaging the growth of iron oxide spherulite nanostructures in real time, characteristics of the radial growth, tip splitting and the reaction front are obtained. Furthermore, a model based on the observed growth kinetics is also established, which helps to develop a quantitative understanding of the spherulite formation mechanisms.

2 Experimental

The growth solution was prepared by dissolving iron nitrate in a solvent mixture of oleylamine, oleic acid, and benzyl ether (4.5:4.5:1 in volume ratio). The precursor solution (150 mg/ml iron nitrate) was loaded into a liquid cell, which was sealed with epoxy before imaging (see details in the Electronic Supplementary Material (ESM)). The growth of iron oxide spherulite nanostructures was initiated by electron beam irradiation of the precursor solution. It is also noted that the liquid thickness varies from the initial liquid thickness (i.e., 100 nm as defined by the liquid cell spacer thickness) during in situ imaging [47] and the growth of spherulite nanostructures has been captured regardless of the liquid thickness variations.

FEI F20 ST Tecnai microscope equipped with a Gatan in situ direct detection camera (K2 IS) was used to record high resolution movies (Movie S1 and S3 in the ESM). A temporal resolution of 2.5 milliseconds and ~2k x ~2k resolution were achieved. The electron beam current density of 4000-8000 $e^-/Å^2 \cdot s$ was used. The K2 IS direct detection camera detects electrons in each pixel by directly exposing a thin CMOS image sensor to the electron beam, which is different from the traditional CCD cameras that use a scintillator to convert electrons to photons. The elimination of scintillator and the corresponding optical fibers has led to significant improvement in both sensitivity and resolution. The output image file was in binary format during recording, later extracted into DigitalMicrograph (DM) format. We also used 3010 JEOL TEM equipped with a Gatan Orius 833 camera to record movies at a rate of 10 frames per second (Movie S2, S4 and S5 in the ESM). An electron beam current density of 5-50 $e^-/Å^2 \cdot s$ was maintained during growth.

A FEI Titan at 200 kV with energy dispersive X-ray mapping (EDS) ChemiSTEM capability was employed for elemental analysis. Prior to EDS mapping, the as-grown liquid cell samples were dried in an ambient environment for several days and then they were opened in order to collect X-ray signals. The images were acquired in STEM mode with a probe convergence semi-angle (α) of 10 mrad. The beam current of 0.3 nA and pixel dwell times between 50 - 100 μs were used. Each map was collected for no more than 60 sec to minimize the electron beam radiation damage.

3 Results and discussion

3.1 Formation of Spherulite Nanostructures and Tip Splitting

The growth of representative iron oxide spherulite nanostructures is shown in Fig. 1. Nanoparticles are formed at the beginning. When several nanoparticles are packed in close proximity, the subsequent radial growth of fibrillar branches from the nanoparticles leads to two-dimensional (2D) spherulite nanostructure formation (spherulite I, as labeled in the third image of Fig. 1(a)). Similar radial growth of fibrillar branches is also observed from a single nanoparticle (spherulite II, as labeled in the third image of Fig. 1(a)). Each nanostructure maintains a nearly 2D circular shape during the course of growth until two adjacent nanostructures meet (Fig. 1(a)). Thickness of 2D spherulite nanostructures is estimated to be 5-6 nm based on the contrast as comparison to the nanoparticle counterpart. The predominant 2D growth mode features heterogeneous nucleation and growth on the SiNx membrane of a liquid cell. The radial 2D growth implies that spherulite nanostructures grow by consuming precursor at the reaction front. Similar spherulite growth behavior is observed in liquid cells with a different liquid thickness and under a different electron beam current density (Fig. S1 and Movie S2 in the ESM).

The development of fibrillar branches (as numbered in Fig. 1(a) at 43.3 s) during the spherulite nanostructure formation is highlighted in Fig. 1(b). Each branch experiences a series of tip splitting events. An initial nanoparticle develops into a number of branches as time elapses (Fig. 1(c)). The branches are densely packed and the spacing between the fibrillar branches is ~ 1 nm. The densely packed fibrillar branches suggest that the growth of each fibrillar branch is highly influenced by the neighboring branches by competing for precursor. As a branch grows wider than a certain value (i.e., an average of 5.8 nm), it splits into two Fig. 1(d). Trajectories of the development of each branch in a spherulite nanostructure is shown in Fig. S2-S3 in the ESM.

In previous studies of spherulites, the width of the fibrillar branches was proposed to be proportional to the diffusion length of impurities in the precursor solution [2]. In this work, the tip splits periodically as the width exceeds a certain value. After a tip splits into two, each develops into a branch growing in the similar direction (unless it encounters a nanoparticle from the secondary nucleation). The tip splitting is consistent with the classical tip splitting theory with respect to instabilities [19, 21, 22, 28, 46]. According to these models, a dendrite tip splits when the tip radius becomes larger than the shortest wavelength of morphological instability. [21] The tip widening and splitting have been observed in the growth of nanodendrites in a liquid cell previously [46]. Here, for direct comparison, we show that using a precursor solution with lower concentration (100 mg/ml) nanodendritic growth has been achieved (Movie S4-S5, Fig. S4-S5 in the ESM and also see previous studies [46]). These results are in agreement with the previous claim [32] that a high oversaturation is required for the spherulite formation.

3.2 Secondary Nucleation and Solid Precipitation

Nanoparticles from secondary nucleation are observed in front of the growing spherulite nanostructures (Fig. 2). Effects of the secondary nanoparticles on the evolution of spherulite nanostructures are highlighted in Fig. 2(a). The tip curvature changes from convex to concave to accommodate the nanoparticle (I & III). If the nanoparticle falls between the tips of two branches (II), the two branches bend to encapsulate the nanoparticle. In all cases, the nanoparticles develop into fibrillar branches at later stage, and become indistinguishable from other primary fibrillar branches in the spherulite nanostructures. Another prominent feature is that there is a layer of solid precipitation at the tip of spherulites during the 2D growth (Fig. 2(b)). The layer thickness increases with the growth of spherulite nanostructure (Fig. 2(c)). It appears that the solid precipitation layer is the same materials as the main spherulite nanostructure but thinner (more details are discussed in Fig. 4).

3.3 The Spherulite Growth Kinetics

In order to quantify the spherulite growth kinetics, changes in the radius (R) of the spherulite with time (t) are plotted. As shown in Fig. 3 (also see Fig. S3 in the ESM), a linear relationship between R and t is obtained at early stage of growth (0-185 s). At later stage we observe a reduction in growth rate and the radius increases nonlinearity in time. Several factors may influence the growth rate of spherulite nanostructures. For example, the activation energy for the attachment of the precursor ions to the fibrillar branches should play a significant role. The precursor concentration (similar to overcooling in other scenarios [14]) and growth temperature are also important parameters. In addition, electron beam intensity, liquid thickness and other factors should also be considered. Based on our measurements as shown in Fig. 3 and previous studies [14, 15], we describe the growth rate (G) relative to the activation energy (ΔE) and temperature (T) as the following:

$$G = G_0 e^{-\Delta E / kT} \qquad (1)$$

where G_0 is a constant depending on the growth conditions and k Boltzmann's constant. Equation (1) explains what we observed in the experiments very well. Since

under certain growth conditions the activation energy and temperature are fixed, a constant growth rate can be achieved. This is consistent with the linear relationship (R~t) in the plots at the early stage of growth.

At the later stage of growth, the growth rate decreases, which may result from various mechanisms. First, the precursor concentration at the reaction front is likely significantly reduced due to secondary nucleation and the solid precipitation at the reaction front as well as the growth of the primary spherulite nanostructure. The reduced precursor concentration may induce growth mode changes. For example, as the growth rate in the early stage is determined by the activation energy, it can be defined as the reaction-controlled growth ($R \sim t$; eq. (1)). However, the nonlinear growth at the later stage (Fig. 3) can be fit to a $R \sim t^{0.5}$ relationship, consistent with diffusion-controlled growth mechanisms (Fig. S6(a) and (b) in the ESM). Second, the decreased precursor concentration may result in changes of the term G_0 in eq. (1). G_0 becomes a variable and it reduces gradually as the oversaturation reduces. Thus, the growth rate decreases as G_0 reduces and various fits of the growth rates at the later stage of growth are shown in Fig. S6(c) and (d) in the ESM. Third, the precipitation layer at the tips of spherulite nanostructures may passivate the 2D growth. Although the precipitation layer is the same material, the thickness of the precipitation layer increases as the spherulites grow. Thus, it is possible that the activation energy for the growth of spherulites increases at the later stage, which may also reduce the growth rate. The onset of nonlinearity in the plots of radius vs time correlates to a precipitated layer thickness of ~ 0.85 nm (in Fig. 2). The grow rate is close to zero at the end, which corresponds to the thickness of a secondary layer larger than 2.7 nm.

3.4 Crystallization of the Spherulite Nanostructures

The spherulite nanostructures are polycrystalline and each fibrillar branch appears to have a preferred crystal orientation. In Fig. 4(a), neighboring single crystalline branches or domains are highlighted in an image frame. The crystal orientation of each fibrillar branch changes during growth (Movie S3 in the ESM). It is noted that in certain image frames the secondary precipitation layer in front of the branches also shows crystal lattice fringes with similar orientation to the primary branches (Fig. 4(b)). Thus, the contrast differences between the solid layer and fibrillar branches suggest thickness variations. In Fig. 4(c), the predominant Fe_3O_4 phase is observed. We also found another crystalline phase, which is ascribed to ferrihydrite ($Fe_{4.8}HO_8 \bullet 4H_2O$). Characterization of additional spherulite nanostructures is shown in Fig. S7 in the ESM. Elemental mapping using energy dispersive X-ray spectroscopy (EDS) of the spherulites (after the growth) shows that iron mostly accumulates in the fibrillar branches while oxygen is found throughout the images (Fig. 4(d)) as oxygen is present in the solution residue as well.

In order to trace the crystalline phase development during the spherulite growth, we identify the crystal phases through the fast Fourier Transform (FFT) of each high resolution image in the movie (Movie S3 in the ESM). The corresponding crystalline domains are highlighted on the original frame by imposing the inverse FFT image (colored) onto the original image. As shown in Fig. 5 (also see Movie S3 in the ESM),

Fe_3O_4 (red) and ferrihydrite (blue) can be clearly identified. Due to the overlapping of some of α-Fe_2O_3 and ferrihydrite lattices (highlighted in green), the α-Fe_2O_3 phase cannot be identified conclusively. The ferrihydrite phase is present in some branches from the early stage and through-out the whole growth process. From the FFT patterns, we plot the d-spacing of each diffraction spot against time labeled with arrows in Fig. 5(b). And, the evolution of different phases during the growth of spherulite nanostructures is shown in Fig. 5(c). The co-existence of ferrihydrite and Fe_3O_4 is a prominent feature of the spherulite nanostructures. The growth of nanostructures with the co-existence of multiple phases can be valuable for various applications.

In order to understand the structural stability of different phases of iron oxide, we have performed additional ex situ experiments. First, the amorphous structure of iron oxide is produced through fast growth of dendritic structures. The faster growth of nanodendrites is likely because the activation barrier for the ion attachment to the amorphous structure is much lower. The growth of amorphous nanodendrites is distinctly different from the polycrystalline spherulite formation. The nanodendritic growth is controlled by ion diffusion in the solution (Fig. S8 in the ESM). As reported in a previous study [46], the fast growth leads to more significant instabilities at the growing tip, resulting in more open, less compact structures (Fig. S2 in the ESM). We find that the amorphous iron oxide branches in nanodendrites can be converted into a crystalline structure under either electron beam irradiation or thermal heating [46]. As shown in Fig. S9 in the ESM, a mixture of Fe_3O_4 (magnetite) and ferrihydrite have been achieved under mild heating of an amorphous iron oxide, i.e., 40 ºC for about 10-20 days. With further heating of the structure, a pure Fe_3O_4 phase is obtained. From the above in situ and ex situ experiments, we conclude that Fe_3O_4 phase is the more stable phase. The crystallization of Fe_3O_4 may be achieved through two possible pathways: (1) ferrihydrite as the intermediates; (2) direct formation of magnetite. The transformation of amorphous iron oxide to magnetite has been noted previously in the study of iron oxide nanoparticles [48]. Previous reports have also shown that ferrihydrite transforms into magnetite by dehydration and structural rearrangement in presence of excess iron [49-51].

4 Conclusions

In conclusion, we have directly observed the polycrystalline iron oxide spherulite nanostructure formation with high spatial and temporal resolution using liquid cell TEM. Spherulite nanostructure shows a constant rate of growth at the early stage and the growth rate declines at the later stage. The characteristics of tip growth, the reaction front, and crystallization pathways are also obtained. We have further established a growth model to explain the growth kinetics. The fact that the spherulite nanostructures formed in a liquid cell exceedingly resemble the macroscopic spherulites in the literature [52] suggests that there are common rules for such hierarchical nanostructure formation and that our in situ study with liquid cell TEM reveals the growth mechanisms. This work opens opportunities to explore the formation of many other hierarchical nanostructures.

Acknowledgements

This project was supported by the U.S. Department of Energy (DOE), Office of Science, Office of Basic Energy Sciences (BES), Materials Sciences and Engineering Division under Contract No. DE-AC02-05-CH11231 within the in-situ TEM (KC22ZH) program. Work at the Molecular Foundry was supported by the Office of Science, Office of Basic Energy Sciences, of the U.S. Department of Energy under Contract No. DE-AC02-05CH11231. We acknowledge Gatan Inc. for the advanced K2 IS camera and Dr. Ming Pan and Dr. Cory Czarnik for their help with part of experimental set up in this work. W. Z. acknowledges the support from Tianjin University Graduate School International Academic Exchange Fund. M. R. H. was funded by KAUST project under H.Z. at UC Berkeley.

Electronic Supplementary Material: Supplementary material (e.g., experimental detail, additional in situ movie analysis) is available in the online version of this article at http://dx.doi.org/10.1007/s12274-***-****-* (automatically inserted by the publisher).

References

[1] Geveling, N.; Maslenkov, S. Solidification of eutectic Ni-Ni_3Ti alloys. *Met. Sci. Heat Treat.* **1976**, *18*, 755-760.

[2] Crist, B.; Schultz, J. M. Polymer spherulites: A critical review. *Prog. Polym. Sci.* **2016**, *56*, 1-63.

[3] Kolosov, V. Y.; Shvamm, K.; Gainutdinov, R.; Tolstikhina, A. Combined TEM-AFM study of “transrotational” spherulites growing in thin amorphous films. *Bull. Russ. Acad. Sci.: Physics* **2007**, *71*, 1442-1446.

[4] Sasaki, N.; Murakami, Y.; Shindo, D.; Sugimoto, T. Computer simulations for the growth process of peanut-type hematite particles. *J. Colloid Interface Sci.* **1999**, *213*, 121-125.

[5] Fowler, A.; Berger, B.; Shore, M.; Jones, M.; Ropchan, J. Supercooled rocks: Development and significance of varioles, spherulites, dendrites and spinifex in Archaean volcanic rocks, Abitibi Greenstone belt, Canada. *Precambrian Res.* **2002**, *115*, 311-328.

[6] Davis, B. K.; McPhie, J. Spherulites, quench fractures and relict perlite in a Late Devonian rhyolite dyke, Queensland, Australia. *J. Volcanol. Geotherm. Rec.* **1996**, *71*, 1-11.

[7] Hutter, J. L.; Bechhoefer, J. Three classes of morphology transitions in the solidification of a liquid crystal. *Phys. Rev. Lett.* **1997**, *79*, 4022-4025.

[8] Hutter, J. L.; Bechhoefer, J. Morphology transitions in diffusion-and kinetics-limited solidification of a liquid crystal. *Phy. Rev. E* **1999**, *59*, 4342-4352.

[9] Hutter, J. L.; Bechhoefer, J. Banded spherulitic growth in a liquid crystal. *J. Cryst. Growth* **2000**, *217*, 332-343.

[10] Kim, Y. Y.; Ribeiro, L.; Maillot, F.; Ward, O.; Eichhorn, S. J.; Meldrum, F. C. Bio-inspired synthesis and mechanical properties of calcite-polymer particle composites. *Adv. Mater.* **2010**, *22*, 2082-2086.

[11] Toda, A.; Okamura, M.; Taguchi, K.; Hikosaka, M.; Kajioka, H. Branching and higher order structure in banded polyethylene spherulites. *Macromolecules* **2008**, *41*, 2484-2493.

[12] Maxfield, J.; Mandelkern, L. Crystallinity, supermolecular structure, and thermodynamic properties of linear polyethylene fractions. *Macromolecules* **1977**, *10*, 1141-1153.

[13] Voigt-Martin, I.; Mandelkern, L. A quantitative electron microscopic study of the crystallite structure of molecular weight fractions of linear polyethylene. *J. Polym. Sci. Ploym. Phys. Ed.* **1984**, *22*, 1901-1917.

[14] Magill, J. Review spherulites: A personal perspective. *J. Mater. Sci.* **2001**, *36*, 3143-3164.

[15] Keith, H.; Padden Jr, F. Spherulitic crystallization from the melt. II. Influence of fractionation and impurity segregation on the kinetics of crystallization. *J. Appl. Phys.* **1964**, *35*, 1286-1296.

[16] Asta, M.; Hoyt, J.; Karma, A. Calculation of alloy solid-liquid interfacial free energies from atomic-scale simulations. *Phys. Rev. B* **2002**, *66*, 100101.

[17] Karma, A.; Rappel, W.-J. Numerical simulation of three-dimensional dendritic growth. *Phys. Rev. Lett.* **1996**, *77*, 4050-4053.

[18] Karma, A.; Rappel, W.-J. Quantitative phase-field modeling of dendritic growth in two and three dimensions. *Phy. Rev. E* **1998**, *57*, 4323-4349.

[19] Langer, J. S. Instabilities and pattern formation in crystal growth. *Rev. Mod. Phys.* **1980**, *52*, 1-28.

[20] Morris, J. R. Complete mapping of the anisotropic free energy of the crystal-melt interface in Al. *Phys. Rev. B* **2002**, *66*, 144104.

[21] Mullins, W. W.; Sekerka, R. Stability of a planar interface during solidification of a dilute binary alloy. *J. Appl. Phys.* **1964**, *35*, 444-451.

[22] Mullins, W. W.; Sekerka, R. F. Morphological stability of a particle growing by diffusion or heat flow. *J. Appl. Phys.* **1963**, *34*, 323-329.

[23] Plapp, M.; Karma, A. Multiscale random-walk algorithm for simulating interfacial pattern formation. *Phys. Rev. Lett.* **2000**, *84*, 1740-1743.

[24] Plapp, M.; Karma, A. Multiscale finite-difference-diffusion-monte-carlo method for simulating dendritic solidification. *J. Comput. Phys.* **2000**, *165*, 592-619.

[25] Provatas, N.; Goldenfeld, N.; Dantzig, J. Efficient computation of dendritic microstructures using adaptive mesh refinement. *Phys. Rev. Lett.* **1998**, *80*, 3308–3311.

[26] Sun, D.; Asta, M.; Hoyt, J. Kinetic coefficient of Ni solid-liquid interfaces from molecular-dynamics simulations. *Phys. Rev. B* **2004**, *69*, 024108.

[27] Sun, D.; Mendelev, M.; Becker, C.; Kudin, K.; Haxhimali, T.; Asta, M.; Hoyt, J.; Karma, A.; Srolovitz, D. Crystal-melt interfacial free energies in hcp metals: A molecular dynamics study of Mg. *Phys. Rev. B* **2006**, *73*, 024116.

[28] Turing, A. The chemical basis of morphogenesis. *Phil. Trans. R. Soc. Lond. B* **1952**, *237*, 37-72.

[29] Sperling, L. H. *Introduction to physical polymer science*; John Wiley & Sons: New Jersey, 2006.

[30] Magill, J.; Plazek, D. Physical properties of aromatic hydrocarbons. II. Solidification behavior of 1, 3, 5-tri-α-naphthylbenzene. *J. Chem. Phys.* **1967**, *46*, 3757-3769.

[31] Muthukumar, M. Commentary on theories of polymer crystallization. *Eur. Phys. J. E: Soft Matter Biol. Phys.* **2000**, *3*, 199-202.

[32] Gránásy, L.; Pusztai, T.; Tegze, G.; Warren, J. A.; Douglas, J. F. Growth and form of spherulites. *Phy. Rev. E* **2005**, *72*, 011605.

[33] Aaronson, H.; Spanos, G.; Masamura, R.; Vardiman, R.; Moon, D.; Menon, E.; Hall, M. Sympathetic nucleation: An overview. *Mater. Sci. Eng. B* **1995**, *32*, 107-123.

[34] Ferrone, F. A.; Hofrichter, J.; Sunshine, H. R.; Eaton, W. A. Kinetic studies on photolysis-induced gelation of sickle cell hemoglobin suggest a new mechanism. *Biophys. J.* **1980**, *32*, 361-380.

[35] Ferrone, F. A.; Hofrichter, J.; Eaton, W. A. Kinetics of sickle hemoglobin polymerization: II. A double nucleation mechanism. *J. Mol. Biol.* **1985**, *183*, 611-631.

[36] Samuel, R. E.; Salmon, E.; Briehl, R. W. Nucleation and growth of fibres and gel formation in sickle cell haemoglobin. *Nature* **1990**, *345*, 833-835.

[37] Galkin, O.; Vekilov, P. G. Mechanisms of homogeneous nucleation of polymers of sickle cell anemia hemoglobin in deoxy state. *J. Mol. Biol.* **2004**, *336*, 43-59.

[38] Liao, H.-G.; Zheng, H. Liquid cell transmission electron microscopy. *Annu. Rev. Phys. Chem.* **2016**, *67*, 719-747.

[39] Kim, B. J.; Tersoff, J.; Kodambaka, S.; Reuter, M. C.; Stach, E. A.; Ross, F. M. Kinetics of individual nucleation events observed in nanoscale vapor-liquid-solid growth. *Science* **2008**, *322*, 1070-1073.

[40] Harutyunyan, A. R.; Chen, G. G.; Paronyan, T. M.; Pigos, E. M.; Kuznetsov, O. A.; Hewaparakrama, K.; Kim, S. M.; Zakharov, D.; Stach, E. A.; Sumanasekera, G. U. Preferential growth of single-walled carbon nanotubes with metallic conductivity. *Science* **2009**, *326*, 116-120.

[41] Ross, F. M. Opportunities and challenges in liquid cell electron microscopy. *Science* **2015**, *350*, aaa9886.

[42] Zheng, H. M.; Smith, R. K.; Jun, Y. W.; Kisielowski, C.; Dahmen, U.; Alivisatos, A. P. Observation of single colloidal platinum nanocrystal growth trajectories. *Science* **2009**, *324*, 1309-1312.

[43] Liao, H.-G.; Cui, L.; Whitelam, S.; Zheng, H. Real-time imaging of Pt3Fe nanorod growth in solution. *Science* **2012**, *336*, 1011-1014.

[44] Liao, H.-G.; Zherebetskyy, D.; Xin, H.; Czarnik, C.; Ercius, P.; Elmlund, H.; Pan, M.; Wang, L.-W.; Zheng, H. Facet development during platinum nanocube growth. *Science* **2014**, *345*, 916-919.

[45] Wang, Y.; Peng, X.; Abelson, A.; Xiao, P.; Qian, C.; Yu, L.; Ophus, C.; Ercius, P.; Wang, L.-W.; Law, M.; et al. Dynamic deformability of individual PbSe nanocrystals during superlattice phase transitions. *Sci. Adv.* **2019**, *5*, eaaw5623.

[46] Hauwiller, M. R.; Zhang, X.; Liang, W.-I.; Chiu, C.-H.; Zhang, Q.; Zheng, W.; Ophus, C.; Chan, E. M.; Czarnik, C.; Pan, M.; et al. Dynamics of nanoscale dendrite formation in solution growth revealed through in situ liquid cell electron microscopy. *Nano Lett.* **2018**, *18*, 6427-6433.

[47] Yang, J.; Zeng, Z.; Kang, J.; Betzler, S.; Czarnik, C.; Zhang, X.; Ophus, C.; Yu, C.; Bustillo, K.; Pan, M.; et al. Formation of two-dimensional transition metal oxide nanosheets with nanoparticles as intermediates. *Nat. Mater.* **2019**, *18*, 970–976.

[48] Baumgartner, J.; Dey, A.; Bomans, P. H.; Le Coadou, C.; Fratzl, P.; Sommerdijk, N. A.; Faivre, D. Nucleation and growth of magnetite from solution. *Nat. Mater.* **2013**, *12*, 310-314.

[49] Tronc, E.; Belleville, P.; Jolivet, J. P.; Livage, J. Transformation of ferric hydroxide into spinel by iron (II) adsorption. *Langmuir* **1992**, *8*, 313-319.

[50] Benner, S. G.; Hansel, C. M.; Wielinga, B. W.; Barber, T. M.; Fendorf, S. Reductive dissolution and biomineralization of iron hydroxide under dynamic flow conditions. *Environ. Sci. Technol.* **2002**, *36*, 1705-1711.

[51] Hansel, C. M.; Benner, S. G.; Neiss, J.; Dohnalkova, A.; Kukkadapu, R. K.; Fendorf, S. Secondary mineralization pathways induced by dissimilatory iron reduction of ferrihydrite under advective flow. *Geochim. Cosmochim. Acta* **2003**, *67*, 2977-2992.

[52] Müller, C.; Aghamohammadi, M.; Himmelberger, S.; Sonar, P.; Garriga, M.; Salleo, A.; Campoy-Quiles, M. One-step macroscopic alignment of conjugated polymer systems by epitaxial crystallization during spin-coating. Adv. Funct. Mater. **2013**, 23, 2368-2377.

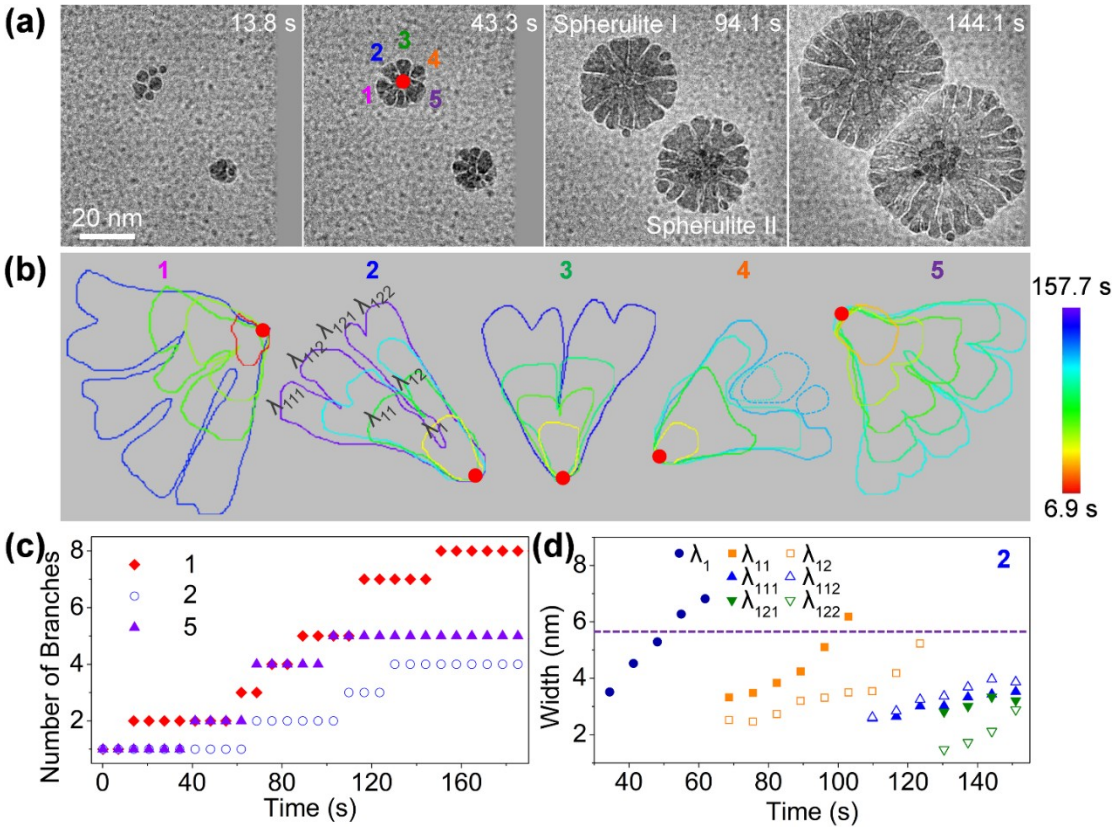

Figure 1 Formation of iron oxide spherulite nanostructures from a molecular precursor solution. (a) Sequential images show the growth of two spherulite nanostructures. Spherulite I and Spherulite II are highlighted in the third image (at 94.1s). (b) Contour plots showing the development of fibrillar branches from nanoparticles at the initial stage (corresponding to those highlighted in a). (c) The number of branches with time for the three highlighted branches in (b) showing the tip splitting behavior. (d) For a selected branch, the width evolution of an individual branch with time. It shows the branch splits when it reaches an average of 5.8 nm.

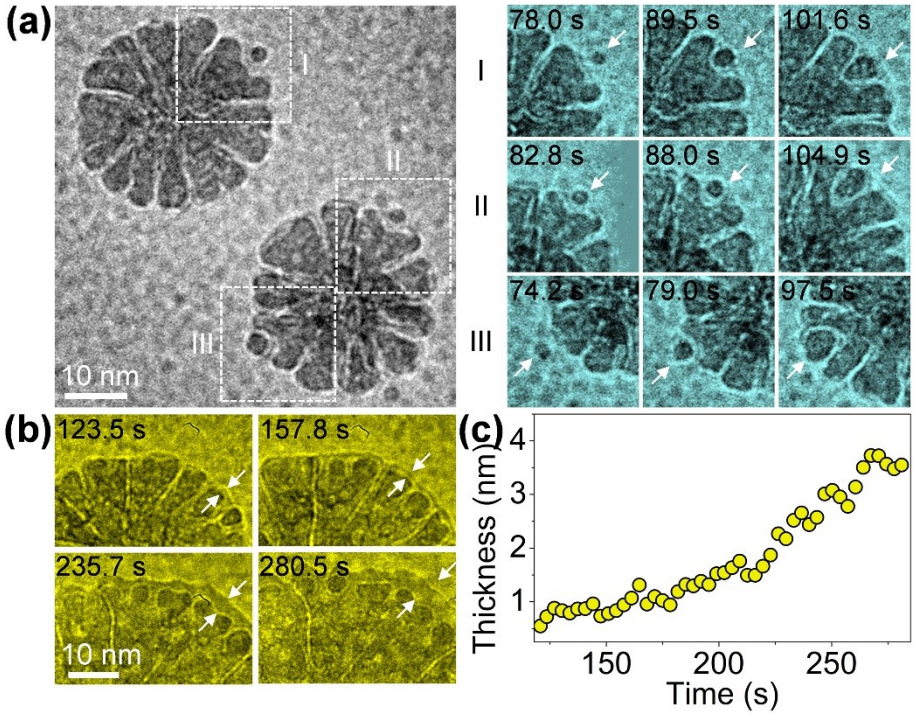

Figure 2 Reaction front of the spherulite nanostructures. (a) Nanoparticles from secondary nucleation at the reaction front develop into fibrillar branches of a spherulite nanostructure. (b) A layer of solid precipitates at the front of the spherulite nanostructure and it grows thicker with time. (c) The solid precipitate layer thickness evolution in (b) with time.

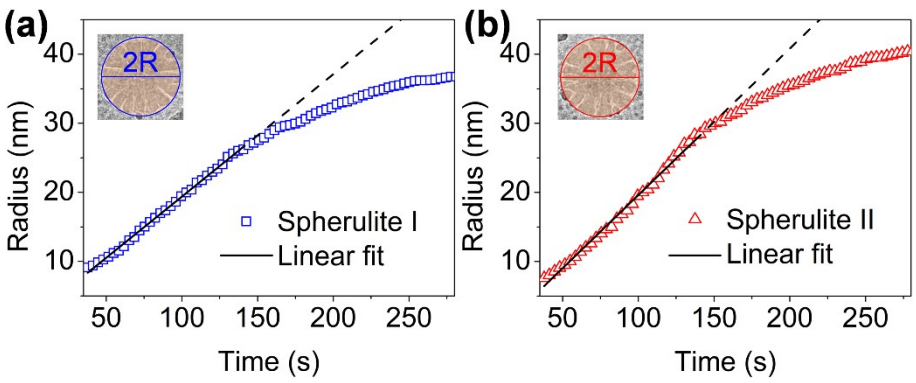

Figure 3 Spherulite radius vs time. Two spherulite nanostructures as highlighted in Figure1A were measured: (A) spherulite I and (B) spherulite II.

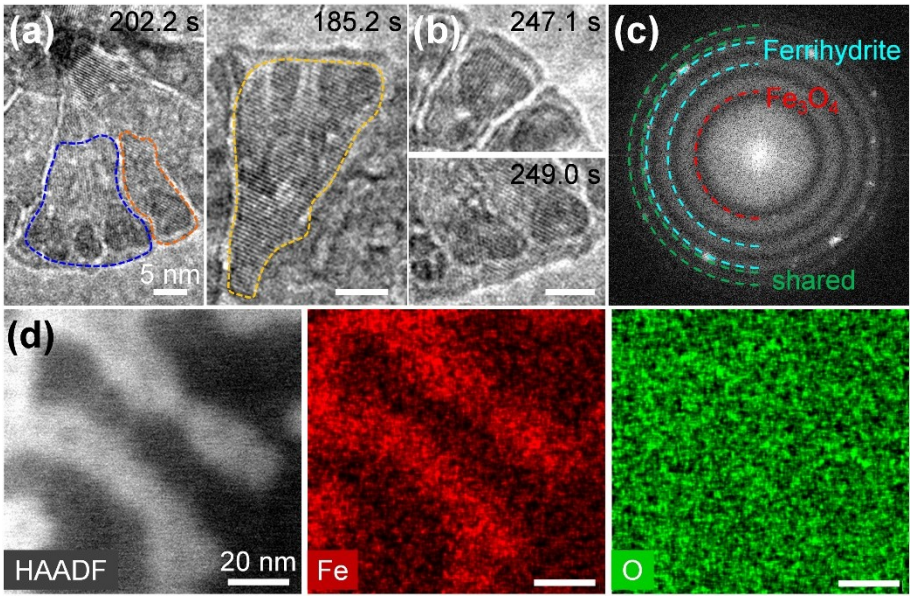

Figure 4 Structural and chemical analysis of the spherulite nanostructure. (a) High resolution TEM images with the highlighted single crystalline domains. (b) High resolution TEM images show that the layer of solid precipitates at the tip is crystalline and shares the same crystal lattice orientation. (c) Fast Fourier transform (FFT) pattern of the spherulite nanostructures at the later stage indicates they are polycrystalline. (d) High angle annular dark field scanning TEM (HAADF-STEM) image and the corresponding energy dispersive X-ray spectroscopy (EDS) maps showing the Fe and O elemental distribution in a spherulite nanostructure. As oxygen presents both in the spherulite nanostructure and in the residue solution, no distinct feature is observed in the O elemental map.